ACS APPLIED ELECTRONIC MATERIALS

Open Access

pubs.acs.org/acsaelm

Article

Strain-Engineered Ge/SiGe Resonant Tunneling Diodes for Silicon-Based Terahertz Emitters

Damiano Marian, Enrico Talamas Simola,* Marco Leone, Elia Bonistalli, Abdulraoof I. A. Ali, Luciana Di Gaspare, Giovanni Capellini, Monica De Seta, Stefano Roddaro, and Michele Virgilio

Cite This: ACS Appl. Electron. Mater. 2026, 8, 5830−5839

Read Online

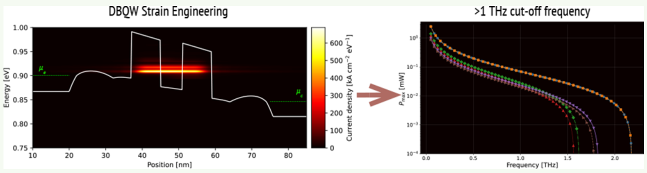

ABSTRACT: We present a comprehensive theoretical study of n-type Ge/SiGe resonant tunneling diodes integrated on Si substrates, aimed at developing CMOS-compatible terahertz oscillators. Leveraging non-equilibrium Green's function simulations combined with semi-analytical modeling, we investigate the influence of band structure engineering, strain, and heterostructure composition on device performance. Optimal double-barrier quantum well profiles are identified within experimentally feasible constraints, highlighting a trade-off between the device current density and the current peak-to-valley ratio (PVR) in the negative differential resistance (NDR) region of the *J*–*V* characteristic. Optimized designs feature PVRs of up to ∼10 at low current densities or, alternatively, higher current densities of up to 100 kA/cm^2 accompanied by lower PVR values. Predicted cut-off frequencies exceed 1 THz, with output powers on the order of tenths of milliwatts. Furthermore, a drift-based model highlights the importance of lateral bias uniformity in mesa devices, setting critical design limits for stable negative differential resistance behavior. These results indicate the potential of Ge/SiGe resonant tunneling diodes as a viable route toward silicon-integrated THz electronic sources, bridging the gap between III–V and group-IV semiconductor platforms.

KEYWORDS: *SiGe, CMOS compatibile, THz, resonant tunneling diode, NEGF*

■ INTRODUCTION

Over the past decades, the lack of powerful and efficient sources emitting radiation in the THz spectral region, the so-called "THz gap", has motivated considerable research efforts driven by the relevance of this frequency range in a number of practical applications.[1] Two complementary routes have been proposed to address the insufficient power emitted by devices operating around 1 THz. One approach involves increasing the operating frequency of microwave emitters, which are typically based on microelectronic oscillating circuits. The other approach aims at increasing the wavelength of the radiation emitted by light-emitting devices, such as quantum cascade lasers.

Despite numerous attempts and several noteworthy proposals, the 'THz gap' still hinders the widespread implementation of emitters and detectors operating in the far- and mid-infrared ranges. A THz platform has yet to achieve the technological maturity and cost-effectiveness required for mass production. Aiming to close the THz gap from the "electronic side", oscillating circuits based on CMOS-compatible electronic devices represent a promising alternative toward relatively compact and cost-effective solutions capable of continuous-wave (CW) THz generation, possibly also at room temperature (RT). State-of-the-art technologies have already increased the operating frequency of SiGe heterojunction bipolar transistors (HBTs) to several hundreds of GHz, enabling high-performance mm- and sub-mm-wave applications.[2] Using the same platform, even larger frequencies can be envisioned leveraging on active elements featuring negative differential resistance (NDR), as demonstrated in III–V-based devices operating up to the THz range. In this case, the oscillating behavior is controlled by the electrical instability related to the NDR effect, which can be engineered in unipolar resonant tunneling diodes (RTDs) by exploiting the bias dependence of the tunneling rate through a double-barrier quantum well (DBQW).

Conceived as an evolution of the Esaki tunnel diode (TD)[3] to overcome its frequency limitation (confined to the X-band or lower due to its high associated capacitance[4,5]), the unipolar RTD remains the fastest demonstrated solid-state semiconductor electronic device operating at room temperature (RT).[6] It can drive oscillators whose fundamental frequency approaches 2 THz[7] and whose output power reaches the mWatt level in the J-band (220–325 GHz).[8] Oscillating circuits based on this device architecture have been developed using several III–V

Received: March 9, 2026
Revised: June 26, 2026
Accepted: June 29, 2026
Published: July 13, 2026

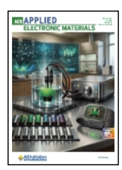

https://doi.org/10.1021/acsaelm.6c00440
ACS Appl. Electron. Mater. 2026, 8, 5830−5839

material platforms, for instance, GaAs/AlGaAs, GaAs/AlAs, and InGaAs/AlAs. More recently, III-nitrides have also gained interest in the THz RTD community despite the low quality of the Ohmic contacts demonstrated so far and the large effective mass, which reduces the tunneling rate, thus limiting the maximum operation frequency.[9–12]

In the past, RTDs have also been demonstrated in CMOS technology using n-type Si-rich SiGe/Si strained heterostructures, following the pioneering work of ref 13, mainly by Paul and co-workers,[14,15] who proposed SiGe RTDs as active elements for fabricating low-power static random access memories.[16] However, owing to the relatively low Si electron mobility and the large tunneling effective mass along the [001] direction of the Si Δ_2 band edge, Si-rich SiGe/Si RTDs are doomed to under-perform their III–V counterparts. Similar material parameter constraints pose an upper boundary to the maximum frequency expected in hole-based SiGe RTD devices as well.[17]

A viable alternative for realizing fast, CMOS-compatible RTD devices could be based on n-type Ge-rich Ge/SiGe heterostructures, thanks to their lighter tunneling mass associated with the L-point conduction minima. This has a positive impact on the maximum oscillation frequency since it induces faster tunneling times, lowering the quantum capacitance of the device. Moreover, from a material growth perspective, because the transmission coefficient depends exponentially on both mass and barrier thickness, a lighter carrier effective mass relaxes the requirements for ultra-thin tunneling barriers. Thus, a given tunneling current can be obtained with thicker and, hence, more reproducible barrier layers.

Over the past two decades, continuous progress in the epitaxy of Ge-rich Ge/SiGe heterostructures grown on Si substrates has unlocked the potential of this material platform for silicon photonics applications such as guiding, emitting, and detecting light in the near-, mid-, and far-infrared spectra.[18–23] Furthermore, Ge-rich Ge/SiGe heterostructures are also attracting interest from the research communities in quantum computing, spintronics, thermoelectrics, and microelectronics, all contributing to the renaissance of Ge as a 'new old' material.[20]

In this paper, we use advanced numerical simulations to theoretically investigate the potential of n-type RTD devices based on a Ge/SiGe DBQW for use in fast oscillating devices. First, to optimize the DBQW potential defined by the L-point band edge of the heterostructure, we identify the subset of compositional profiles of the active multilayer stack that meets the constraints related to experimental feasibility in terms of mechanical stability, available doping range, and minimal layer thicknesses for the tunneling barriers. Subsequently, using the most promising composition profiles, we carried out a systematic campaign of non-equilibrium Green's function (NEGF) calculations by tuning the geometrical degree of freedom of the DBQW to simulate and optimize the RTD *J*–*V* characteristics. We chose the emitted power at 0.5 THz of an oscillating circuit having the SiGe/Ge RTD as an active element as the figure of merit. Finally, we used the *J*–*V* responses predicted by the NEGF simulations in conjunction with a semi-analytical model to investigate non-idealities in vertical RTD devices, caused by in-plane inhomogeneities in the voltage distribution. Remarkably, this analysis reveals that the lateral dimensions of the mesa structure must not exceed well-defined constraints to preserve the NDR in the *I*–*V* characteristic of the device.

■ RESULTS AND DISCUSSION

Double-Barrier QW Profiles with n-Type Ge/SiGe Heterostructure

The physics governing the non-linear electric response of an RTD diode is schematically depicted in Figure 1a, together with the notation introduced to describe the diode's non-linear *J*–*V* characteristics.

To optimize the NDR non-linear effect, the coupling of the confined states with the plane waves in the emitter and collector regions has to be accurately engineered by tuning the thicknesses and heights of the tunneling barriers. This is challenging due to the limited band offset existing in the conduction band of Ge-rich SiGe heterostructures and to their complex character, given the presence of different band minima. In fact, unstrained $Si_{1-x}Ge_x$ alloys features two sets of conduction band valleys at similar energies: a six-fold degenerate one at the Δ point and a four-fold degenerate one at *L*. The absolute conduction band minimum changes from the former to the latter as the Ge content x increases beyond the $x^* = 0.85$ threshold.[24] This effect limits the available range of Ge concentrations to $x > x^*$ in the SiGe barrier material when engineering the L-point conduction band profile of Ge-rich heterostructures.

Under in-plane biaxial strain, the x^* value increases, detrimentally reducing the available band offset. The increase of x^* is due to the impact of lattice deformation on the electronic levels, which causes the splitting of the six-fold degenerate Δ states into Δ_2 and Δ_4 levels due to the tetragonal distortion imposed by heteroepitaxy. SiGe barriers typically experience some amount of tensile strain: this strain is controlled by the virtual substrate (VS) composition y, which sets the in-plane lattice constant in the multilayer stack and is typically chosen at an intermediate value x_{avg} between x_{well} and x_{bar} to allow strain compensation of the entire structure, thereby avoiding dislocation-mediated plastic relaxation.[25] This epitaxial strain adds to the tensile thermal strain arising from the different coefficients of thermal expansion featured by the Si substrate and the Ge-rich epilayers,[26] resulting in a further increase of x^*. However, recent studies[27] have questioned the strain compensation constraint, deliberately setting $y < x_{avg}$ to compensate for the thermal tensile strain and/or reduce the Δ splitting, effectively reducing x^*.

The L-point band offset at the barrier/well interface for $x \sim 0.8$ is found to be approximately 130 meV,[28] lower than the offsets found in both III–V and Si-rich Si/SiGe systems, yet sufficient to engineer robust quantum confinement effects.[21,29,30] As previously mentioned, the conduction band profile when $x \simeq x^*$ (see Figure 1b) is complicated by the presence of Δ states in the barriers, close in energy to the L edge. This results in a reduction of the exploitable SiGe/Ge band offset, as evidenced in the left region of Figure 1c, where we display the calculated conduction band offset as a function of x and y in the [0.7, 1] and [0.8, 1] ranges, respectively. The Δ profile may entail a parallel conduction channel and/or increase the conductance of the L one due to interband L–Δ scattering mechanisms at the well/barrier interfaces involving states confined in the SiGe layers, thus effectively lowering the barriers and worsening the RTD figure of merit.

Given the complexity of this scattering channel and the lack of related literature, the simplest approach would be to set $x > x^*$ throughout the heterostructure, perhaps by lowering x^* and relinquishing strain compensation to achieve larger band

https://doi.org/10.1021/acsaelm.6c00440
ACS Appl. Electron. Mater. 2026, 8, 5830–5839

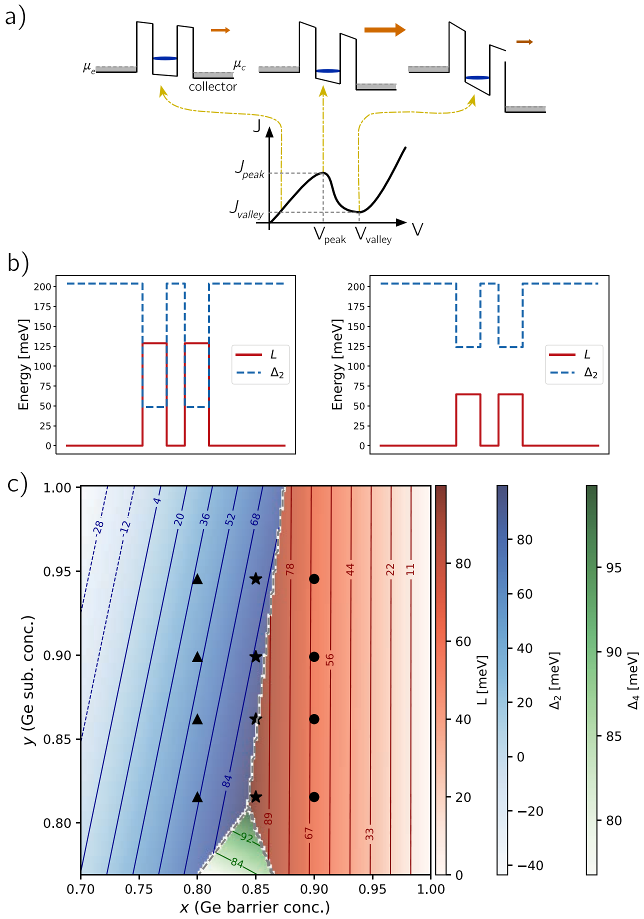

Figure 1. (a) Schematic band profile of an RTD device at different biases, linked to the corresponding points in the J–V characteristic. μ_e (μ_c) is the Fermi energy in the emitter (collector) region, the blue area between the two barries represents the DBQW confined level, and the orange arrows represent the intensity of the current. Applying a bias V across the structure, a peak J_{peak} in the J–V curve occurs when the energy of the electrons in the emitter reservoir aligns with the confined level in the well and the resonant tunneling mechanism takes place. (b) Energy profiles for the L (red solid) and Δ_2 (blue dashed) band edges in a $Si_{1-x}Ge_x$/Ge DBQW, grown on a fully relaxed $Si_{0.09}Ge_{0.91}$ virtual substrate for $x = 0.8$ (left) and $x = 0.9$ (right). (c) Band offset at the barrier-well interface as a function of the Ge concentration in the VS (y) and barrier (x) alloy material. The offsets in the blue, red, and green regions are controlled by the energies of the Δ_2, L, and Δ_4 barrier levels, respectively. Solid symbols mark the sets of parameters chosen for the NEGF simulations. Here and in the following, the thermal contribution to the biaxial strain in the heterostructure (see text) is calculated at the lattice temperature of 77 K assuming complete relaxation of the VS. Further details regarding the calculations of conduction band offsets are reported in the Supporting Information, alongside the full set of necessary material parameters in Table S2.

offsets (see the red region on the right of Figure 1c). As a particular case, we observe that choosing $x = 0.85$ would require fully relaxed barriers. To this aim, the y content of the VS must be chosen to be <0.85 to compensate for the tensile thermal strain at the operating temperature. For instance, at 77 K and assuming a perfectly relaxed VS, one obtains $y \simeq 0.81$. It is important to note that any residual tensile strain in the VS due to incomplete epitaxial relaxation should be taken into account, as this would lower y even further. Despite the significant variation in Ge concentration between the VS and the heterostructure, the nucleation of additional misfit dislocations should be minimal due to the heterostructure's limited thickness.

J–*V* Characteristic and Active Region Optimization

To assess and optimize the transport properties of SiGe/Ge RTD devices, designed in light of the band edge profiles discussed in the previous section, we use the self-consistent NEGF method, as implemented in the NextNano software suite. The considered carrier scattering mechanisms are alloy, electron–electron, charged impurity, electron–phonon, and interface roughness[31] and have been modeled relying on the literature values of the material parameters collected in the NextNano default database. The non-ideality of the SiGe/Ge heterointerface is described in terms of RMS roughness and lateral correlation length, estimated according to the accurate structural analysis reported in ref 32. The numerical values for such parameters are summarized in Table S1.

Both elastic and inelastic scattering events impact the width of the transmission resonance, thus degrading the peak-to-valley ratio (PVR),[33−35] while sequential tunneling mediated by the e-ph interaction may cause a voltage shift in the onset of the NDR region.[36] It is to be noted that electron–phonon scattering is expected to be weaker in group-IV-based heterostructures with respect to their III–V counterparts, due to the non-polar character of their lattice. The weaker e-ph interaction, on one hand, is beneficial since it increases the device robustness against temperature variations, but, on the other hand, results in lower thermalization rates for hot electrons, whose energy makes them insensitive to the double-barrier potential.[37]

We first focus on the low-lattice-temperature regime (T = 77 K), leaving the investigation of the thermal stability of the device to the end of the section. We have selected three values for the Ge content x in the barrier (solid symbols), combining them with different substrate concentrations (y = 0.81, 0.86, 0.90, and 0.95), corresponding to the 12 black markers shown in Figure 1c. In the first set, we consider a barrier composition $x = 0.90$ (circle symbol), corresponding to Δ valleys in the barrier region above the L ones, thus avoiding any influence of the Δ states on the transport properties. In the second set (stars symbol), we fix $x = 0.85$, which ensures a larger band offset for the L-band edge profile across all substrate concentrations. However, for this Ge content, the Δ edges in the barrier have lower energy and, when this layer is tensile strained ($y > x$), are found below the L level, transitioning from the red to the blue region of Figure 1. Nevertheless, the quantum confinement of the Δ subband states in the barrier layers lifts their energy above the SiGe L-point. Consequently, also for $x = 0.85$, L–Δ scattering is expected to have a limited impact on transport, allowing us to describe it relying on a single-band framework. Finally, in the third set of conditions (triangle symbols), we further decrease the Ge content in the barriers ($x = 0.80$) to maximize the L-point band offset. At this concentration the Δ edge falls below the L-band in the barrier region, reducing the accuracy of single-band calculations. In this case, it is likely that the L–Δ scattering channel may detrimentally influence the resonant tunneling of L electrons, in principle requiring a multiband approach to model the device. Nevertheless, it should also be noted that the energy offset between the $x = 0.80$ barrier and

https://doi.org/10.1021/acsaelm.6c00440
ACS Appl. Electron. Mater. 2026, 8, 5830−5839

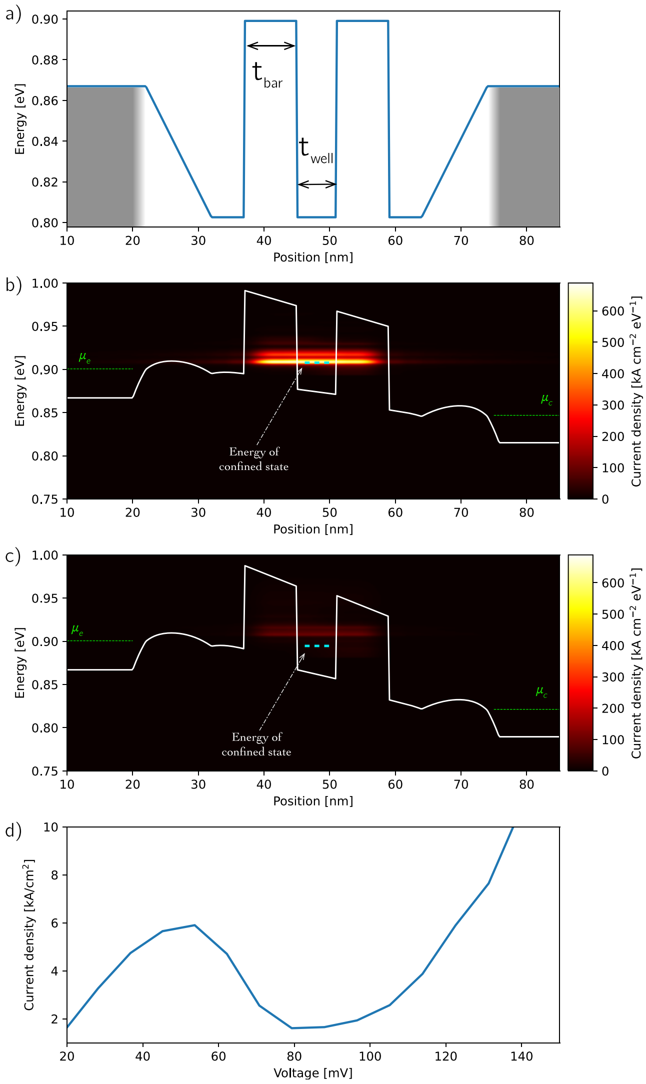

Figure 2. (a) Complete L-point band edge profile including two graded regions on both sides of the DBQW for a typical RTD design featuring $x = 0.85$, $y = 0.86$, $t_{bar} = 8$ nm, and $t_{well} = 6$ nm. The gray areas in the n^{++} emitter and collector regions schematically evidence the presence of a concentration tail, related to the unintentional diffusion of dopants. (b) Energy and spatially resolved current density at 77 K, calculated at the peak voltage $V_{peak} = 54$ mV. The chemical potentials in the contacts (green) and the energy of the confined DBQW (blue) are also shown. (c) As in (b) but at a valley bias of $V_{valley} = 80$ mV. The current maps of (b) and (c) are shown in the DBQW region only. (d) *J*–*V* characteristic for the same device geometry.

the well at the Δ edge is in the range of 40–90 meV, thus providing an effective barrier for the Δ_2 carriers.

In Figure 2a, we show an exemplary case of the DBQW L-band edge profile. The corresponding choice of design parameters is reported in the caption. The Ge content in the n^{++} collector and emitter regions, featuring a doping concentration of 1×10^{19} cm^{-3}, is set equal to that of the substrate. As in refs [15,16], we have embedded the DBQW with two 17 nm-thick undoped layers, including a 10 nm graded region whose Ge content linearly varies between the one in the emitter/collector region and $x = 1$, and a 5 nm $x = 1$ layer next to the barrier. The grading partially compensates for the electrostatic effects stemming from the accumulation of electrons reflected by the barriers, thus lowering the bias required to achieve the peak current.[14] The undoped regions are thick enough to prevent the diffusion-driven dopant tail from reaching the graded regions. In fact, relying on secondary ion mass spectrometry (SIMS) data,[38] the P donor profile has been modeled by an error function with $\sigma = 8$ nm. The shape of the self-consistent band profiles evidences charge accumulation in the graded layers, as shown in Figure 2b,c where the energy and spatially resolved density current at the peak and valley voltages are also displayed, respectively. For this design, the *J*–*V* characteristic (see panel d) features a peak (valley) current of 5.9 (1.6) kA cm^{-2} at V_{peak} (V_{valley}) equal to 54 (80) mV, corresponding to a PVR of 3.7. Notice that, at 77 K, the valley current is dominated by non-resonant tunneling with a larger spread in energy with respect to the one observed at V_{peak}. Indeed, at this temperature, charge transport above the barrier level is found to be negligible, despite the relatively modest SiGe/Ge band offset of the DBQW.

To optimize device performance, for each (x, y) pair, we simulate the RTD *J*–*V* characteristic by varying both the barrier and well thicknesses in the ranges $t_{bar} \in [6–9]$ nm and $t_{well} \in [4–6]$ nm, respectively. As a figure of merit, we aim to maximize the maximum achievable RF emission power at 0.5 THz, i.e., $P_{max}(f = 0.5\ \text{THz})$, which is a function of the PVR, ΔV, and current density J (see eq 2 below in this section).

The calculated PVR and J_{peak} values are reported in Figure 3 (solid points) as functions of the concentration of Ge in the barrier x and in the substrate y. Each point shows the optimal design for the specific choice of (x, y), with the corresponding values of t_{well} and t_{bar} specified in the legend. For fixed (x, y), we also report the mean PVRs and J_{peak} as solid lines. The PVR increases upon decreasing x due to the larger band offsets (see panel a), and values are typically found in the 1–8 range, reaching the maximum ratio of 10 at $x = 0.80$ when t_{bar} and t_{well} are set to 8 and 5 nm, respectively (not shown). The predicted PVRs, although well below those achieved by novel 2D material platforms,[39] are comparable with the typical values for III–V-based RTDs.[40] Moreover, according to our simulations, Ge/SiGe RTDs are expected to outperform in terms of PVR with respect to their Si/SiGe counterpart, for which experimental values around 2 have been reported in the literature.[15,16]

As for J_{peak}, we observe that higher x values lead to larger peak currents, which however are generally accompanied by lower PVRs. We attribute this effect mainly to the impact of x on the thermionic contribution to the total current, brought about by the reduction of the band offset, resulting in larger valley currents. For the chosen design geometries, the current densities shown in Figure 3b are typically of the order of several tens of kA/cm^2, a range enabling the design of THz emitters featuring reasonable output powers. The largest peak current is ∼270 kA cm^{-2}, with a PVR of ∼1.6, obtained for both $y = 0.81$ and $y = 0.86$, setting $x = 0.9$, $t_w = 4$ nm, and decreasing the tunneling barrier to 6 nm. This large electrical conductivity hinders the practical application of a uniform vertical bias in mesa devices featuring a large footprint. We will address this point in detail in the subsequent section. Finally, Figure 3 evidences (quasi-)monotonic trends upon varying the y content, whose influence on the PVR (J_{peak}) is greater at low (high) x barrier concentrations. Indeed, y has little influence on the barrier's height, its main role being the tuning of the energy

https://doi.org/10.1021/acsaelm.6c00440
ACS Appl. Electron. Mater. 2026, 8, 5830–5839

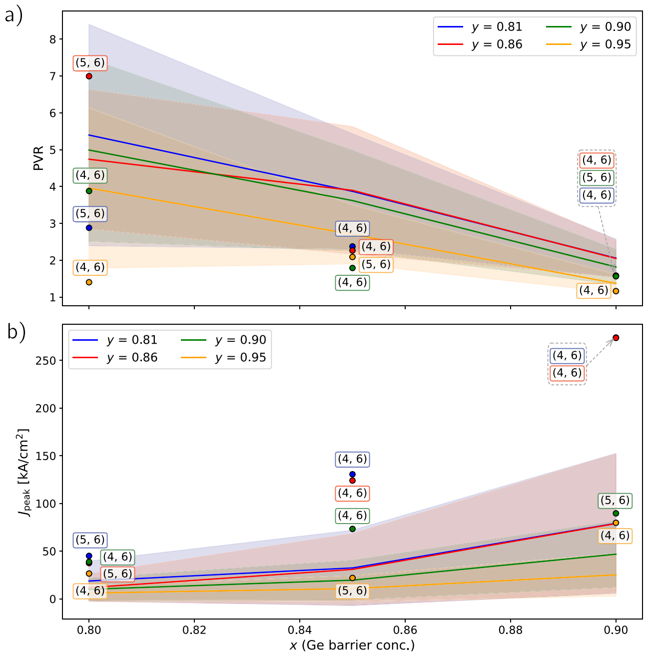

Figure 3. PVR (a) and J_{peak} (b) as functions of the x Ge concentration in the barriers for the optimal designs (points) whose geometrical parameters are explicitly indicated specifying the (t_{well}, t_{bar}) thicknesses in nm. Solid lines represent the mean PVR (a) and J_{peak} (b) values at given x and y concentrations, obtained by averaging over the set of devices characterized by different well and barrier thicknesses; the associated standard deviation is evidenced by the colored shadow regions. Different colors refer to the y Ge content in the substrate specified in the legend.

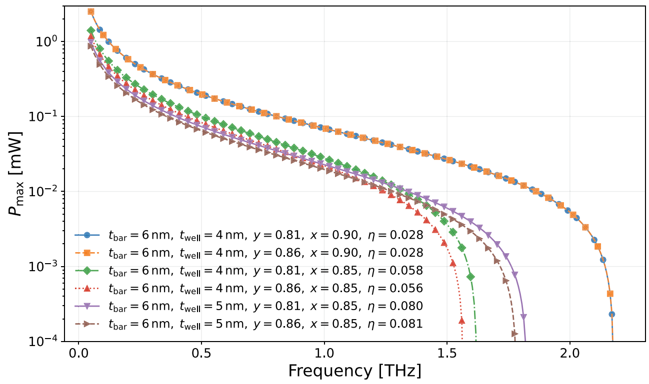

Figure 4. Upper theoretical limit for the emitted power P_{max} as a function of the operating frequency, calculated at 77 K for the optimal (see text) six device designs.

difference between the band edge in the emitter and the confined state in the Ge well.

In RTD-based oscillators, the maximum frequency, f_{max}, defined as the frequency at which the real part of the RTD admittance vanishes due to the NDR roll-off caused by the DBQW electron lifetime, is given by $f_{max} = 1/(2\pi\tau_{DBQW})$, where τ_{DBQW} is the quasi-bound state lifetime.[40] However, in our Ge/SiGe platform, the relatively small conduction band offset makes the barriers quite transparent. This results in a strong coupling between the quantum well and the contacts, yielding a broad resonance peak and a short quasi-bound state lifetime ($\tau_{DBQW} \approx 0.04$ ps, as extracted from equilibrium LDOS simulations). Since the corresponding intrinsic frequency limit ($f_{DBQW} \approx 4$ THz) is higher than the targeted operating ones, the quantum well relaxation time accounts for a negligible fraction of the RF cycle and can be reasonably neglected. Thus, assuming $\tau_{DBQW} \approx 0$, f_{max} becomes limited by the J–V characteristic and the geometrical capacitance, which dominates over its quantum counterpart. In this regime, f_{max} is given by the following simplified expression:[41]

$$f_{max} = \frac{1}{2\pi R_D C_D}\sqrt{\frac{R_D}{R_S} - 1} \quad (1)$$

where C_D is the diode geometrical capacitance associated with the charging of the RTD contacts, and $R_D = \frac{\Delta V}{\Delta I}$, with $\Delta V = |V_{peak} - V_{valley}|$ and $\Delta I = I_{peak} - I_{valley}$. Thus, the frequency cut-off is now controlled by the $R_S C_D$ charging/discharging time associated with the external load R_S. In real-world RTD oscillating circuits, the frequency constrain posed by R_S is typically more stringent than the one set by the DBQW lifetime, and then f_{max} corresponds to the frequency at which the NDR is canceled out by the equivalent circuit resistance. R_S is usually dominated by the contact resistance. It follows that the fabrication of high-quality Ohmic contacts featuring very low resistivity is a key ingredient for reaching the THz frequency domain. State-of-the-art metal contacts for n-Ge can achieve resistivities of $\simeq 10^{-7}$ Ω cm^2.[42] Using $R_S = 1 \times 10^{-7}$ Ω cm^2 in eq 1 for our optimal designs, and calculating C_D for RTD devices with a diameter d of 5 μm, we get $f_{max} \gtrsim 1$ THz.

The upper theoretical limit for the power P_{max} at frequency f that can be delivered to a load is given by[41]

$$P_{max} = \eta \Delta I \Delta V = \frac{\Delta I^2}{16\pi} \cdot \frac{L}{A\varepsilon_0\varepsilon_r} \cdot \left(\frac{1}{f} - \frac{1}{f_{max}}\right) \quad (2)$$

where L is the length of the intrinsic region, A is the diode area, and η is an efficiency factor, which can be estimated as:[43]

$$\eta = \frac{1}{2}\frac{\left(\frac{J_{peak}}{J_{valley}} - 1\right)\left(\frac{V_{valley}}{V_{peak}} - 1\right)}{\left(\frac{J_{peak}}{J_{valley}} + 1\right)\left(\frac{V_{valley}}{V_{peak}} + 1\right)} \quad (3)$$

In Figure 4, using eqs 2 and 3, we plot P_{max} as a function of the operating frequency for our six best devices with $d = 5$ μm. The design specifications are reported in the legend together with the calculated efficiency η. For this choice of device diameter, f_{max} cannot exceed $\simeq$2.4 THz, and most of the explored designs exhibit a rapid drop of P_{max} above 1.5 THz. The emitted power at 1 THz reaches several tens of μW.

THz emitters based on RTDs are generally more robust against temperature with respect to quantum cascade lasers, where the excitation of the phonon field quenches the population inversion between the two laser levels. However, as mentioned in the Introduction section, the limited band offset featured by n-type SiGe/Ge RTDs may hinder RT operation. At this temperature, the energy of thermally excited incoming carriers is of the same order of the barrier height, resulting in a reduced sensitivity to the DBQW profile. Consequently, the resonance due to tunneling is smeared out upon increasing T,

https://doi.org/10.1021/acsaelm.6c00440
ACS Appl. Electron. Mater. 2026, 8, 5830−5839

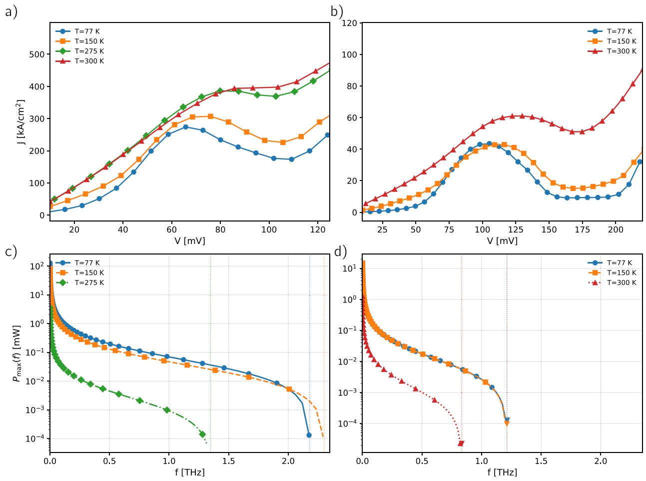

Figure 5. *J*–*V* characteristic at different lattice temperatures (a, b) and corresponding maximum emitted power P_{max} as a function of the operation frequency (c, d). Data refer to the optimal design of Figure 4 featuring $x = 0.90$ (a, c) and to the same design but with barrier Ge content $x = 0.8$ (b, d).

quenching the NDR effect, which may completely disappear before reaching 300 K, as shown in the top-left panel of Figure 5. The data reported there refer to the optimal design corresponding to the blue curve of Figure 4, featuring $x = 0.9$ and resulting in a barrier height of 65 meV only. The PVR decreases from 1.58 at 77 K down to 1.05 at 275 K and vanishes above this temperature. The bottom-left panel of Figure 5 summarizes the impact of the thermally driven quenching of the NDR on both f_{max} and P_{max}.

The high emitted power at low temperature primarily results from the large current density, achieved at the cost of a relatively low peak-to-valley ratio, rendering this configuration particularly sensitive to temperature increases. Therefore, higher energy barriers are required to ensure that the NDR effect persists at and above room temperature. Hence, we analyzed the thermal robustness of the device using the same geometrical parameters and *y* content, while setting $x = 0.80$ (right panels in Figure 5), which increases the band offset to ∼130 meV. This results in a higher PVR (4.8) and a lower $J_{peak} = 4.3 \times 10^4$ A/cm^2 value at 77 K, leading to suboptimal low-temperature emission at 0.5 THz ($P_{max} = 0.016$ mW), which is nevertheless preserved up to 300 K ($P_{max} = 0.001$ mW), where the PVR is 1.2 and $J_{peak} = 6.1 \times 10^4$ A/cm^2. Thus, accurate device engineering is required to manage the trade-off between the PVR and the current density, which controls the power emitted by the device and its thermal stability.

Bias Distribution in Realistic Mesa Devices and Its Impact on *J*–*V* Response

The Ge/SiGe RTD devices studied here typically consist of a thin mesa structure, where the active intrinsic DBQW region is sandwiched between highly doped (n^{++}) Ge-rich SiGe layers serving as top and bottom contact regions (Figure 6a). A critical constraint arises from CMOS-compatible processing, limiting the active dopant concentration to approximately 1–2 × 10^{19} cm^{-3}.[44,45] Given the small thickness of these n^{++} layers, their in-plane resistance can be non-negligible. At the same time, despite its much lower conductivity, the DBQW region may

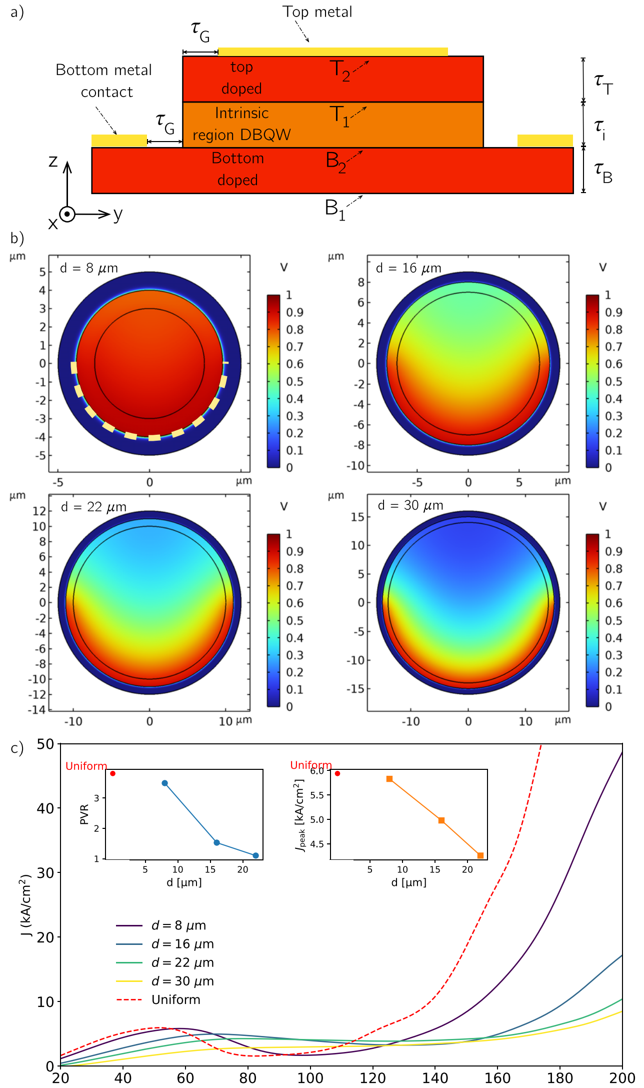

Figure 6. (a) Schematic of the mesa structure studied in this section. Relevant geometrical parameters and orientation of the reference system are indicated. (b) In-plane distribution of the potential difference Φ in cylindrical RTD devices featuring a metal contact on the top surface and a grounded bottom one, placed along half perimeter (dotted yellow curve), biased at 1 V. Mesa diameters vary from 8 to 30 μm. (c) Corresponding *J*–*V* characteristics, compared with the one calculated assuming a uniform bias in the mesa area; in the inset, the PVR and the spatially averaged *J*, estimated at the diameter dependent V_{peak} point are also reported as a function of *d*. Design parameters are detailed in the caption of Figure 2.

exhibit high cross-plane conductance due to its large area and small thickness. As a consequence, the parasitic voltage drop within the doped layers can easily become comparable to the bias across the resonant tunneling barrier. In large-footprint devices, this may prevent a uniform electrostatic potential $\phi(x, y)$ in the bottom layer, potentially leading to a smearing and eventual suppression of the NDR regime.

While finite-element method (FEM) simulations can be used to estimate such a bias distribution, the extremely low aspect ratio of these devices makes 3D FEM computationally expensive. Thus, we developed a semi-analytical steady-state drift model based on the hypothesis that the conductivities of the n^{++} (σ_{dop}) and

https://doi.org/10.1021/acsaelm.6c00440
ACS Appl. Electron. Mater. 2026, 8, 5830−5839

DBQW (σ_i) regions are vastly different and satisfy $\sigma_{dop} \gg \sigma_i$. As a consequence, at every given position (x, y), the potential $\phi(x, y, z)$ is expected to be approximately constant as a function of z within the top and bottom layers, with a voltage drop occurring almost entirely across the DBQW. Within this intrinsic region, the potential profile can be assumed to be approximately linear, with a predominantly vertical current flow (see SI for a numerical verification). In this limit, the system can be described in terms of two averaged potentials, $\phi_T(x, y)$ and $\phi_B(x, y)$, in the top and bottom doped layers. Under steady-state conditions, these are governed by the coupled continuity equations

$$\begin{cases} \nabla_{xy}\cdot[-\sigma_T^{(2D)}\nabla_{xy}\phi_T(x,y)] &= -J_{z,T_2} + J_{z,T_1} \\ \nabla_{xy}\cdot[-\sigma_B^{(2D)}\nabla_{xy}\phi_B(x,y)] &= -J_{z,B_2} + J_{z,B_1} \end{cases} \quad (4)$$

where $\nabla_{xy} = (\partial_x, \partial_y)$, $\sigma_T{}^{2D}$ ($\sigma_B{}^{2D}$) is the 2D conductivity of the top (bottom) contact layer, obtained by multiplying the 3D conductivity by the layer thickness, and the current density J_z is evaluated at the two top (T_1,T_2) and bottom (B_1,B_2) interfaces of the doped layers (see Figure 6a). The vertical current density in the DBQW is given by

$$J_{z,B_2}(x,y) = J_{z,T_1}(x,y) = -\sigma_i \frac{\phi_T(x,y) - \phi_B(x,y)}{\tau_i} \quad (5)$$

In the following, we consider the simplified limit case in which the top metallic contact covers the entire mesa ($\tau_G = 0$). In the pillar region, we expect $J_{z,B_1}(x, y) = 0$ and $J_{z,T_1}(x, y) = J_{z,T_2}(x, y)$, leading to an in-plane distribution of the vertical bias $\Phi(x, y) = \phi_T(x, y) - \phi_B(x, y)$, completely governed by the spatial variation of $\phi_B(x, y)$, and given by

$$\nabla_{x,y}^2 \Phi = \frac{\Phi}{\lambda^2} \quad (6)$$

where $\lambda = \sqrt{\tau_i \sigma_B^{2D}/\sigma_i}$ emerges as the natural length scale of the problem. The boundary conditions for this differential equation are simply $\Phi(x, y) = V$ at the edge of the mesa, where the metallic contact is located.

We thus conclude that when the lateral dimension of the mesa is comparable to or larger than λ, the in-plane dependence of the vertical bias cannot be neglected. In this case, the actual electrical characteristic of the device for a given applied voltage must be evaluated by averaging the current response over the (x, y) plane, calculated at the local value of the potential difference $\Phi(x, y)$.

To quantitatively assess this effect in our structure, we extrapolate σ_i through a linear fit of the J–V curves, obtaining conductivities of the order of 10^{-1} S/cm. As for the thickness of the intrinsic region, we use $\tau_i \simeq 60$ nm, a representative value for the DBQWs profiles presented in the previous section. Finally, $\sigma_B{}^{2D}$ can be estimated by considering a $\tau_B = 150$ nm-thick n^{++} Ge-rich bottom layer with an active donor concentration of 1×10^{19} cm^{-3}. Using, for this material, $\sigma_{dop} = 5 \times 10^2$ S/cm,[46] we obtain $\sigma_B{}^{2D} \simeq 7.5 \times 10^{-3}$ S, leading to $\lambda = 7$ μm.

With these values, we numerically solved eq 6 for circular RTD devices with a diameter d ranging in the 8–30 μm interval under an external bias of 1 V, assuming a metallic bottom contact placed along half of the perimeter at $\tau_G = 1$ μm (see Figure 6a). The resulting in-plane distribution for Φ is shown in Figure 6b, clearly demonstrating a degradation of the bias uniformity for devices larger than ~8 μm, a value that, as expected, is at the same scale of λ. The accompanying smoothing of the NDR upon enlarging d is evident from the J–V curves reported in Figure 6c, which also suggests a detrimental increase of both V_{peak} and ΔV. In the inset of Figure 6c, we report the PVR as a function of the mesa diameter. From the maximum value of 3.8 corresponding to a perfectly uniform bias, it decreases to 1.52 when $d = 16$ μm and completely disappears above $d = 30$ μm. In line with this result, the effective peak current density J, calculated by averaging over the (x, y) plane, also decreases upon increasing the device footprint (see inset). This trend is a signature of the shrinking of the area affected by the current flow, which in large devices is confined to a narrow region close to the perimeter of the mesa. We believe that this mechanism can explain a similar behavior reported in Figure 3 of ref 47 for the effective J measured in n-type SiGe/Si RTD devices.

To reduce bias inhomogeneities without limiting the device area, one can rely on elongated structures. As an example, here we investigate rectangular stripe geometries, featuring a fixed longitudinal length of 200 μm and a transverse W of 8, 16, 22, and 30 μm. As sketched in Figure 7a, the bottom contact

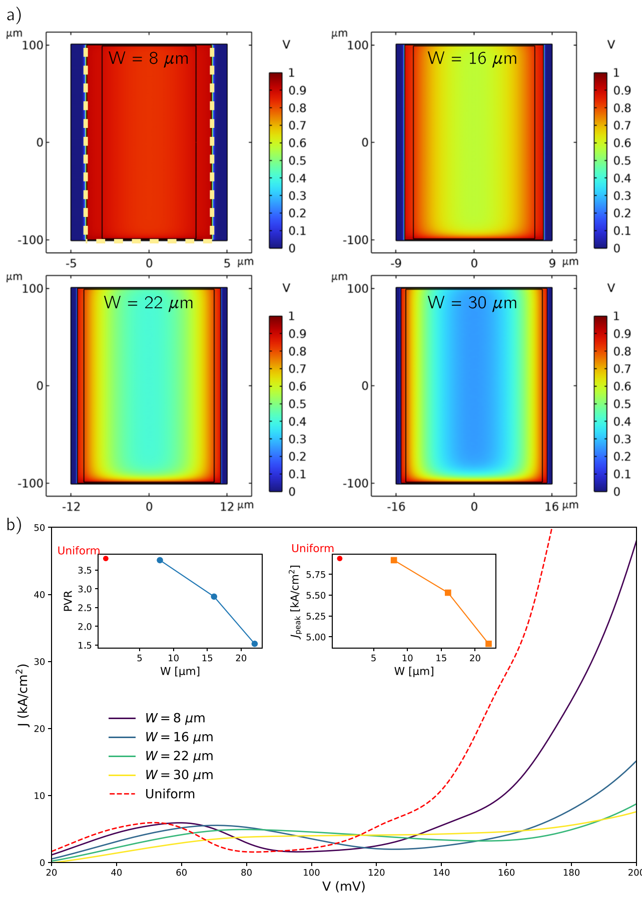

Figure 7. (a) In-plane distribution of the potential difference Φ in rectangular RTD devices featuring a metal contact on the top surface and a U-shaped grounded bottom one (dotted yellow curve), biased at 1 V. The vertical length is fixed at 200 μm, while the transverse one varies from 8 to 30 μm. (b) Corresponding J–V characteristics, compared with the one calculated assuming a uniform bias; in the inset, the PVR and the spatially averaged J, estimated at the W dependent V_{peak} value, are also reported as a function of the transverse width. Design parameters are detailed in the caption of Figure 2.

https://doi.org/10.1021/acsaelm.6c00440
ACS Appl. Electron. Mater. 2026, 8, 5830−5839

is realized by assuming a U-shaped metallic layer which partially surrounds the RTD mesa, placed as before at $\tau_G = 1$ μm. In these devices, bias uniformity along the transverse direction is facilitated by the presence of the metallic regions placed on both sides of the stripe. Non-negligible variations in Φ are observed along the transverse direction when $W \simeq 2\lambda$, leading to a suppression of the NDR regime, similar to the cylindrical case, and to a reduction of the area of the device interested by the current flow, as apparent from the inset in Figure 7b.

■ CONCLUSIONS

In this work, we have theoretically investigated the feasibility of n-type Ge/SiGe RTDs grown on Si substrates with the goal of enabling THz emission in oscillating circuits based on this material platform. To this aim, we have combined band structure engineering and systematic advanced transport calculations within the NEGF formalism, which currently represents the state of the art for the simulation of vertical transport in planar tunneling heterostructures. The theoretical framework fully takes into account both elastic and inelastic scattering channels, by using realistic material input parameters derived from recent literature on the Ge/SiGe system.

This study shows that the current response of optimized Ge-rich RTDs is characterized by well-defined resonant tunneling features. The optimization of the emitted power reveals a clear trade-off between current density and peak-to-valley ratio (PVR): PVR values as high as ∼10 are achieved at the expense of lower current densities, whereas current densities on the order of 10^4–10^5 A/cm^2 are obtained by reducing the barrier thickness, resulting in lower PVR values. Thermal stability analysis indicates that, regardless of the modest L-band offset, the NDR effect can persist up to ∼275 K for barrier compositions around $x = 0.9$, and remains observable at 300 K when the barrier Ge content is reduced to $x = 0.8$. It should be noted, however, that for $x = 0.8$, the proximity of Δ and L bands may lead to intervalley mixing, potentially limiting the actual performance.

From the static J–V response, we estimated cut-off frequencies exceeding 1 THz, thus highlighting the potential of this material system for the realization of compact, CMOS-integrable THz oscillators. Future developments could focus on the possible role of the L–Δ coupling in influencing the resonant transport mechanism and on the impact of lateral bias non-uniformity to further refine the designs suggested here. In conclusion, our work suggests that optimized Ge/SiGe RTDs may provide a viable pathway toward bridging the gap between III–V-based THz compact optical sources and Si-compatible electronics.

■ ASSOCIATED CONTENT

Supporting Information

The Supporting Information is available free of charge at https://pubs.acs.org/doi/10.1021/acsaelm.6c00440.

Mathematical description of the theoretical model for voltage distribution and validation of the model by comparison with FEM simulations; list of material parameters required for simulations and details on the calculations of the conduction band offset (PDF)

■ AUTHOR INFORMATION

Corresponding Author

Enrico Talamas Simola – *Dipartimento di Scienze, Università degli Studi Roma Tre, Viale G. Marconi 446, 00146 Roma, Italy;* orcid.org/0000-0001-5468-6712; Email: enrico.talamassimola@uniroma3.it

Authors

Damiano Marian – *Dipartimento di Fisica "E. Fermi", Università di Pisa, Largo Pontecorvo 3, 56127 Pisa, Italy;* orcid.org/0000-0002-6759-6350

Marco Leone – *Dipartimento di Scienze, Università degli Studi Roma Tre, Viale G. Marconi 446, 00146 Roma, Italy;* orcid.org/0009-0006-1282-6151

Elia Bonistalli – *Dipartimento di Fisica "E. Fermi", Università di Pisa, Largo Pontecorvo 3, 56127 Pisa, Italy*

Abdulraoof I. A. Ali – *Dipartimento di Fisica "E. Fermi", Università di Pisa, Largo Pontecorvo 3, 56127 Pisa, Italy*

Luciana Di Gaspare – *Dipartimento di Scienze, Università degli Studi Roma Tre, Viale G. Marconi 446, 00146 Roma, Italy;* orcid.org/0000-0003-3134-7296

Giovanni Capellini – *Dipartimento di Scienze, Università degli Studi Roma Tre, Viale G. Marconi 446, 00146 Roma, Italy; IHP-Leibniz Institute for High Performance Microelectronics, Im Technologiepark 25, 15236 Frankfurt(Oder), Germany;* orcid.org/0000-0002-5169-2823

Monica De Seta – *Dipartimento di Scienze, Università degli Studi Roma Tre, Viale G. Marconi 446, 00146 Roma, Italy;* orcid.org/0000-0002-8920-8371

Stefano Roddaro – *Dipartimento di Fisica "E. Fermi", Università di Pisa, Largo Pontecorvo 3, 56127 Pisa, Italy;* orcid.org/0000-0002-4707-1434

Michele Virgilio – *Dipartimento di Fisica "E. Fermi", Università di Pisa, Largo Pontecorvo 3, 56127 Pisa, Italy*

Complete contact information is available at: https://pubs.acs.org/doi/10.1021/acsaelm.6c00440

Notes

The authors declare no competing financial interest.

■ ACKNOWLEDGMENTS

D.M. and M.V. warmly thank Riccardo Mannella for the fruitful and stimulating discussions. They also thank Stefan Birner and Thomas Grange for their assistance with the NextNano simulation suite. This work was funded by the Italian MUR under the PRIN 2022 PNRR project "Integrable THz Si-based Quantum Cascade Operation", CUP I53D23006680001, funded by the European Union – NextGenerationEU. S.R. also acknowledges for the developement of the model reported in Sec. IV the financial support of the TRUST project (PRIN 2022M5RSK5).

■ REFERENCES

(1) Pavlidis, D., Ed. *Fundamentals of Terahertz Devices and Applications*; Wiley, **2021**.

(2) Fox, A. et al. Advanced Heterojunction Bipolar Transistor for Half-THz SiGe BiCMOS Technology. *IEEE Electron. Device Lett.* **2015**, *36*, 642–644.

(3) Sze, S. M. In *Physics of semiconductor devices*; Wiley, **2006**.

(4) Hornbostel, D. 5-10 Ghz YIG-tuned tunnel-diode oscillator. *Proc. IEEE* **1965**, *53*, 1751–1751.

(5) Nelson, D.; Sterzer, F. Tunnel-diode microwave oscillators with milliwatt power outputs. *WESCON/60 Conference Record*; IEEE, **1960**; pp 68–73.
(6) Feiginov, M. Frequency Limitations of Resonant-Tunnelling Diodes in Sub-THz and THz Oscillators and Detectors. *J. Infrared Millim. Terahertz Waves* **2019**, *40*, 365–394.
(7) Izumi, R.; Suzuki, S.; Asada, M. 1.98 THz resonant-tunneling-diode oscillator with reduced conduction loss by thick antenna electrode. *2017 42nd International Conference on Infrared, Millimeter, and Terahertz Waves (IRMMW-THz)*; IEEE, **2017**; pp 1–2.
(8) Al-Khalidi, A.; Alharbi, K. H.; Wang, J.; Morariu, R.; Wang, L.; Khalid, A.; Figueiredo, J. M. L.; Wasige, E. Resonant Tunneling Diode Terahertz Sources With up to 1 mW Output Power in the J-Band. *IEEE Trans. Terahertz Sci. Technol.* **2020**, *10*, 150–157.
(9) Zhang, W. D.; Growden, T. A.; Brown, E. R.; Berger, P. R.; Storm, D. F.; Meyer, D. J. Fabrication and Characterization of GaN/AlN Resonant Tunneling Diodes. *High-Frequency GaN Electronic Devices*; Springer: Cham, **2020**, 249–281.
(10) Growden, T. A.; Zhang, W.; Brown, E. R.; Storm, D. F.; Hansen, K.; Fakhimi, P.; Meyer, D. J.; Berger, P. R. 431 kA/cm^2 peak tunneling current density in GaN/AlN resonant tunneling diodes. *Appl. Phys. Lett.* **2018**, *112*, 033508.
(11) Encomendero, J.; Yan, R.; Verma, A.; Islam, S. M.; Protasenko, V.; Rouvimov, S.; Fay, P.; Jena, D.; Xing, H. G. Room temperature microwave oscillations in GaN/AlN resonant tunneling diodes with peak current densities up to 220 kA/cm^2. *Appl. Phys. Lett.* **2018**, *112*, 103101.
(12) Zhang, H.; Xue, J.; Sun, Z.; Li, L.; Yao, J.; Liu, F.; Yang, X.; Wu, G.; Li, Z.; Fu, Y.; Liu, Z.; Zhang, J.; Hao, Y. 1039 kA/cm^2 peak tunneling current density in GaN-based resonant tunneling diode with a peak-to-valley current ratio of 1.23 at room temperature on sapphire substrate. *Appl. Phys. Lett.* **2021**, *119*, 153506.
(13) Ismail, K.; Meyerson, B. S.; Wang, P. J. Electron resonant tunneling in Si/SiGe double barrier diodes. *Appl. Phys. Lett.* **1991**, *59*, 973–975.
(14) Paul, D. J.; See, P.; Zozoulenko, I. V.; Berggren, K.-F.; Kabius, B.; Holländer, B.; Mantl, S. Si/SiGe electron resonant tunneling diodes. *Appl. Phys. Lett.* **2000**, *77*, 1653–1655.
(15) Suet, Z.; Paul, D. J.; Zhang, J.; Turner, S. G. Si/SiGe n-type resonant tunneling diodes fabricated using in situ hydrogen cleaning. *Appl. Phys. Lett.* **2007**, *90*, 203501.
(16) Ternent, G.; Paul, D. J. Si/SiGe Tunneling Static Random Access Memories. *ECS Trans.* **2013**, *50*, 987–990.
(17) Tsujino, S.; Usami, N.; Weber, A.; Mussler, G.; Shushunova, V.; Grützmacher, D.; Azuma, Y.; Nakajima, K. SiGe double barrier resonant tunneling diodes on bulk SiGe substrates with high peak-to-valley current ratio. *Appl. Phys. Lett.* **2007**, *91*, 032104.
(18) Montesinos-Ballester, M.; Vakarin, V.; Ramirez, J. M.; Liu, Q.; Alonso-Ramos, C.; Roux, X. L.; Frigerio, J.; Ballabio, A.; Barzaghi, A.; Deniel, L.; Bouville, D.; Vivien, L.; Isella, G.; Marris-Morini, D. Optical modulation in Ge-rich SiGe waveguides in the mid-infrared wavelength range up to 11 μm. *Commun. Mater.* **2020**, *1*, 6.
(19) Stark, D.; Mirza, M.; Persichetti, L.; Montanari, M.; Markmann, S.; Beck, M.; Grange, T.; Birner, S.; Virgilio, M.; Ciano, C. et al. THz intersubband electroluminescence from n-type Ge/SiGe quantum cascade structures. *Appl. Phys. Lett.* **2021**, *118*, 101101.
(20) Fischer, I. A.; Brehm, M.; De Seta, M.; Isella, G.; Paul, D. J.; Virgilio, M.; Capellini, G. On-chip infrared photonics with Si-Ge-heterostructures: What is next? *APL Photonics* **2022**, *7*, 050901.
(21) Campagna, E.; Talamas Simola, E.; Venanzi, T.; Berkmann, F.; Corley-Wiciak, C.; Nicotra, G.; Baldassarre, L.; Capellini, G.; Di Gaspare, L.; Virgilio, M.; Ortolani, M.; De Seta, M. High-quality CMOS compatible n-type SiGe parabolic quantum wells for intersubband photonics at 2.5–5 THz. *Nanophotonics* **2024**, *13*, 1793–1802.
(22) Berkmann, F.; Venanzi, T.; Baldassarre, L.; Campagna, E.; Talamas Simola, E.; Di Gaspare, L.; Corley-Wiciak, C.; Capellini, G.; Nicotra, G.; Sfuncia, G. et al. Ultrastrong Coupling of $Si_{1-x}Ge_x$ Parabolic Quantum Wells to Terahertz Microcavities. *ACS Photonics* **2024**, *11*, 2776–2786.
(23) Marris-Morini, D.; Vakarin, V.; Ramirez, J. M.; Liu, Q.; Ballabio, A.; Frigerio, J.; Montesinos, M.; Alonso-Ramos, C.; Roux, X. L.; Serna, S.; Benedikovic, D.; Chrastina, D.; Vivien, L.; Isella, G. Germanium-based integrated photonics from near- to mid-infrared applications. *Nanophotonics* **2018**, *7*, 1781–1793.
(24) Braunstein, R.; Moore, A. R.; Herman, F. Intrinsic Optical Absorption in Germanium-Silicon Alloys. *Phys. Rev.* **1958**, *109*, 695–710.
(25) Talamas Simola, E.; Montanari, M.; Corley-Wiciak, C.; Di Gaspare, L.; Persichetti, L.; Zollner, M. H.; Schubert, M. A.; Venanzi, T.; Cagnon Trouche, M.; Ortolani, M. et al. Subnanometer Control of the Heteroepitaxial Growth of Multimicrometer-Thick Ge/Si-Ge Quantum Cascade Structures. *Phys. Rev. Appl.* **2023**, *19*, 014011.
(26) Capellini, G.; De Seta, M.; Zaumseil, P.; Kozlowski, G.; Schroeder, T. High temperature x ray diffraction measurements on Ge/Si(001) heterostructures: A study on the residual tensile strain. *J. Appl. Phys.* **2012**, *111*, 073518.
(27) Campagna, E.; Talamas Simola, E.; Di Gaspare, L.; Marian, D.; Zoellner, M. H.; Berkmann, F.; Baldassarre, L.; Ortolani, M.; Capellini, G.; Virgilio, M.; De Seta, M. Challenges in modulation doping of n-type Ge/SiGe heterostructures: The role of epitaxial and thermal strain. *APL Mater.* **2025**, *13*, 061112.
(28) Busby, Y.; De Seta, M.; Capellini, G.; Evangelisti, F.; Ortolani, M.; Virgilio, M.; Grosso, G.; Pizzi, G.; Calvani, P.; Lupi, S.; Nardone, M.; Nicotra, G.; Spinella, C. Near- and far-infrared absorption and electronic structure of Ge-SiGe multiple quantum wells. *Phys. Rev. B* **2010**, *82*, 205317.
(29) Ciano, C.; Virgilio, M.; Montanari, M.; Persichetti, L.; Di Gaspare, L.; Ortolani, M.; Baldassarre, L.; Zoellner, M.; Skibitzki, O.; Scalari, G. et al. Control of Electron-State Coupling in Asymmetric Ge/Si-Ge Quantum Wells. *Phys. Rev. Appl.* **2019**, *11*, 014003.
(30) Montanari, M.; Ciano, C.; Persichetti, L.; Corley, C.; Baldassarre, L.; Ortolani, M.; Di Gaspare, L.; Capellini, G.; Stark, D.; Scalari, G.; Virgilio, M.; De Seta, M. THz intersubband absorption in n-type $Si_{1-x}Ge_x$ parabolic quantum wells. *Appl. Phys. Lett.* **2021**, *118*, 163106.
(31) Greck, P.; Birner, S.; Huber, B.; Vogl, P. Efficient method for the calculation of dissipative quantum transport in quantum cascade lasers. *Opt. Express* **2015**, *23*, 6587–6600.
(32) Grange, T.; Mukherjee, S.; Capellini, G.; Montanari, M.; Persichetti, L.; Di Gaspare, L.; Birner, S.; Attiaoui, A.; Moutanabbir, O.; Virgilio, M.; De Seta, M. Atomic-Scale Insights into Semiconductor Heterostructures: From Experimental Three-Dimensional Analysis of the Interface to a Generalized Theory of Interfacial Roughness Scattering. *Phys. Rev. Appl.* **2020**, *13*, 044062.
(33) Bude, J. *Monte Carlo Device Simulation*; Springer: US, **1991**; pp 27–66.
(34) Frensley, W. R. Quantum transport modeling of resonant-tunneling devices. *Solid-State Electron.* **1988**, *31*, 739–742.
(35) Ferry, D. K.; Grubin, H. L. *Modeling of Quantum Transport in Semiconductor Devices*; Academic Press, **1996**; pp 283–448.
(36) Mizuta, H.; Tanoue, T. *The Physics and Applications of Resonant Tunnelling Diodes; Cambridge Studies in Semiconductor Physics and Microelectronic Engineering*; Cambridge University Press, **1995**; pp 53–61.
(37) Grange, T.; Stark, D.; Scalari, G.; Faist, J.; Persichetti, L.; Di Gaspare, L.; De Seta, M.; Ortolani, M.; Paul, D. J.; Capellini, G.; Birner, S.; Virgilio, M. Room temperature operation of n-type Ge/SiGe terahertz quantum cascade lasers predicted by non-equilibrium Green's functions. *Appl. Phys. Lett.* **2019**, *114*, 111102.
(38) Schlipf, J.; Talamas Simola, E.; Berkmann, F.; Capellini, G.; De Seta, M.; Di Gaspare, L.; Fischer, I. A.; Marian, D.; Ortolani, M.; Virgilio, M. in preparation.
(39) Lin, Y.-C.; Ghosh, R. K.; Addou, R.; Lu, N.; Eichfeld, S. M.; Zhu, H.; Li, M.-Y.; Peng, X.; Kim, M. J.; Li, L.-J.; Wallace, R. M.; Datta, S.;

Robinson, J. A. Atomically thin resonant tunnel diodes built from synthetic van der Waals heterostructures. *Nat. Commun.* **2015**, *6*, 7311.

(40) Cimbri, D.; Wang, J.; Al-Khalidi, A.; Wasige, E. Resonant Tunneling Diodes High-Speed Terahertz Wireless Communications - A Review. *IEEE Trans. Terahertz Sci. Technol.* **2022**, *12*, 226–244.

(41) Paul, D. J. Si/SiGe heterostructures: from material and physics to devices and circuits. *Semicond. Sci. Technol.* **2004**, *19*, R75.

(42) Gallacher, K.; Velha, P.; Paul, D. J.; MacLaren, I.; Myronov, M.; Leadley, D. R. Ohmic contacts to n-type germanium with low specific contact resistivity. *Appl. Phys. Lett.* **2012**, *100*, 022113.

(43) Haddad, G. I.; East, J. R.; Eisele, H. Two-Terminal Active Devices for Terahertz Sources. *Int. J. High Speed Electron. Syst.* **2003**, *13*, 395–427.

(44) Barget, M. R.; Virgilio, M.; Capellini, G.; Yamamoto, Y.; Schroeder, T. The impact of donors on recombination mechanisms in heavily doped Ge/Si layers. *J. Appl. Phys.* **2017**, *121*, 245701.

(45) Vohra, A.; Makkonen, I.; Pourtois, G.; Slotte, J.; Porret, C.; Rosseel, E.; Khanam, A.; Tirrito, M.; Douhard, B.; Loo, R.; Vandervorst, W. Source/Drain Materials for Ge nMOS Devices: Phosphorus Activation in Epitaxial Si, Ge, $Ge_{1-x}Sn_x$ and $Si_yGe_{1-x-y}Sn_x$. *ECS J. Solid State Sci. Technol.* **2020**, *9*, 044010.

(46) Cuttriss, D. B. Relation Between Surface Concentration and Average Conductivity in Diffused Layers in Germanium. *Bell Syst. Tech. J.* **1961**, *40*, 509–521.

(47) Paul, D. J.; See, P.; Zozoulenko, I. V.; Berggren, K.-F.; Holländer, B.; Mantl, S.; Griffin, N.; Coonan, B. P.; Redmond, G.; Crean, G. M. n-type Si/SiGe resonant tunnelling diodes. *Mater. Sci. Eng. B* **2002**, *89*, 26–29.

https://doi.org/10.1021/acsaelm.6c00440
ACS Appl. Electron. Mater. 2026, 8, 5830–5839